Crystallographic anisotropy of the superelastic and mechanical properties of the Ti-20Zr-3Mo-3Sn alloy evidenced by nanoindentation at the grain scale

Y. Zhou, A. Fillon, D. Laille, T. Gloriant

Crystallographic anisotropy of the superelastic and mechanical properties of the Ti-20Zr-3Mo-3Sn alloy evidenced by nanoindentation at the grain scale

Y. Zhou, A. Fillon*, D. Laillé, T. Gloriant

Univ Rennes, INSA Rennes, CNRS, ISCR-UMR 6226, F-35000, Rennes, France

* Corresponding author: Amélie Fillon

Postal address: Univ Rennes, INSA Rennes, CNRS, ISCR-UMR 6226, 20 avenue des Buttes de Coësmes

E-mail address: amelie.fillon@insa-rennes.fr (A. Fillon).

Abstract:

Nanoindentation was combined with electron backscatter diffraction (EBSD) to investigate the crystallographic anisotropy of indentation responses of individual grains in the superelastic Ti2033 alloy. The high statistic of measurements from grains oriented over a large range of crystallographic directions facilitated a fundamental study covering the entire stereographic triangle of the β phase. For a highlighted visual effect, results were presented as inverse pole figure distribution maps of depth recovery, work recovery, indentation modulus and hardness. Results showed that the pronounced anisotropy behaviors of indentation modulus, depth and work recovery ratios resulted from the anisotropy in Young's modulus and in compressive lattice distortion between the bcc structure of β phase and the orthorhombic structure of the stress-induced α'' martensite phase, respectively. However, orientation dependence was gone when plasticity occurred. The orientation-independency in indentation hardness was due to the various slip systems that might be activated within bcc crystals.

Keywords: Titanium alloys; Nanoindentation; Electron backscattered diffraction; superelasticity; mechanical anisotropy; martensitic transformation.

1. Introduction

Superelasticity and mechanical properties of Ti alloys significantly depends on the crystallographic orientation [1-4]. Uniaxial tensile tests on single crystals oriented in $<100>_{\beta}$, $<110>_{\beta}$ and $<111>_{\beta}$ for metastable β-Ti alloys were realized by Zhang et al. [5] and showed a clear crystallographic anisotropy of the superelasticity and mechanical responses. Currently, compression pillars have also been used to investigate the local material properties at micron and submicron length scales which rely strongly upon miniaturized specimens [6, 7]. Knowledge of orientation-dependent behavior in superelastic Ti alloys is highly desirable in order to optimize the mechanical performances of functional devices to meet the requirements for any proposed applications. To broaden these experimental studies covering more crystallographic directions in the β-Ti crystals, a large number of differently oriented single crystals would be necessary. However, tremendous resources with regard to specimen preparations prohibit extensive testing programs [8]. On the other hand, nanoindentation, when combined with suitable analysis methods, has the potential to become an efficient tool to provide desired information on the anisotropic performances at significantly lower resources and cost at micrometer or nanometer scale [7, 9-13].

Recently, nanoindentation has been also used to investigate the superelastic effect [14-19]. When the nanoindentation platform is coupled with optical microscopy, the targeted indent locations can be chosen visibly and precisely [10]. As such, a large number of nanoindentations can be performed on individual grains with a wide variety of crystal orientations in polycrystalline materials [9, 20], which is particularly feasible to investigate the anisotropic properties of polycrystalline materials at grain scale. The information on anisotropy of the superelasticity, hardness and elastic modulus at grain scale can be of great interest to understand and predict the influences of texture on the macroscopic properties of engineering alloys. However, only a few concerned experimental studies exist in literature.

Polycrystalline β-metastable Ti-20Zr-3Mo-3Sn alloy (at.%; abbreviated as Ti2033) was investigated in the present work. According to the results in earlier work in our group [21], Ti2033 alloys exhibited good superelasticity with a high strain recovery of 3.5% after solution-treated at 1123 K for 0.5 h, and the effect of texture on the superelasticity of Ti2033 were studied by macroscale tensile test experiments. In the present study, nanoindentation was employed to characterize the local mechanical properties within individual grains for which orientations were known from prior electron backscattered diffraction (EBSD) mapping. The strategy of coupling nanoindentation with EBSD was to explore the crystallographic anisotropy of the indentation responses in individual grains of β Ti2033

polycrystalline alloy.

2. Materials and methods

The Ti2033 alloy was elaborated using cold crucible levitation melting (CCLM) of pure raw materials. The synthesized button-shape ingots were then homogenized at 1223 K for 20 h, 90 % cold-rolled, recrystallized at 1073 K for 0.5 h, and water-quenched, so as to retain the β-metastable phase with appropriate grain size and random texture having all possible crystal orientations.

The phase composition was analyzed by x-ray diffraction (XRD) using a Bruker D8 Advance XRD system with Cu Kα radiation operated at 40 kV and 40 mA over the 2θ range of 36° - 95° with a step size of 0.02° and a scanning speed of 0.2°/min. The morphology and grain size was observed by optical microscopy. The crystallographic orientations of individual grains were identified by electron back-scattered diffraction (EBSD) analyses on a JEOL JSM 6400 scanning electron microscope equipped with a TSL EBSD system using an accelerating voltage of 20 kV, a working distance of 15 mm, and a step size of 4 μm. Data were analyzed using CHANNEL 5 software package. The specimens were prepared by electrochemical polishing in an electrolyte composed of perchloric acid (4 vol. %) and methanol (96 vol. %) with a controlled temperature of -14 ~ -16 °C and a controlled electric current of 0.2 A for 45 s. Surface roughness (Ra) was measured by atomic force microscopy (AFM).

Nanoindentation tests were performed on grains with the size larger than 50 μm along the surface normal direction using two indenters: a spherical indenter with a radius of 50 μm (Sp50) and a Berkovich (Bkv) indenter. The two indenters have been calibrated on fused silica. Individual grains with defined orientations by EBSD were located by optical microscopy attached to the instrumented nanoindentation test system. To minimize the influence of grain boundaries and neighboring grains, nanoindentation tests were performed at approximately central area of each targeted grain. A large number of nanoindentation measurements were performed on individual grains to explore their superelastic responses (depth recovery ratio η_h and work recovery ratio η_w) and mechanical properties (indentation hardness H_{IT} and indentation modulus E_{IT}). Measured results were presented in the [001]-[101]-[111] standard stereographic triangles based on the inverse pole figure (IPF) in surface normal direction (ND, parallel to the indentation direction), in order to build the distribution maps (η_h - , η_w - , E_{IT} - and H_{IT} - IPF), which could correlate the mechanical properties with the crystallographic orientation of a given individual grain. Note that the points in η_h - , η_w - , E_{IT} - and H_{IT} - IPFs were positioned according to the orientation

positions of measured grains in the EBSD IPF in ND, and their colors were scaled according to the measured values. Each colored point was related to an average value of at least five measurements.

3. Results and discussion

3.1 Microstructural characterizations

The XRD profile in Fig. 1a displays the (011), (002), (112), (202) and (013) reflections corresponding to the bcc β-Ti polycrystalline structure. Figs. 1b-d present the optical microscope image, EBSD orientation map and the corresponding IPF in ND referring to the same studied area. It shows a typical equiaxed β-grain microstructure with average diameter of 70 μm and randomly distributed orientations, and grain boundaries can be evidently observed. It also demonstrates that individual grains identified by EBSD can be selected correspondingly by optical microscopy just before proceeding to nanoindentation measurements. It is worth noting that the optical microscope image was acquired at a slight underfocus to highlight the grain boundaries. The surface roughness (Ra) measured by AFM is as low as 8.4 nm suggesting that the electrochemically polished surface is in a high quality for nanoindentation measurements.

The analyzed region contains hundreds of grains for which the orientation covers the whole IPF, which allows a substantial study on the orientation dependence of the superelasticity, indentation modulus and indentation hardness at the grain scale in the superelastic β Ti2033 alloy. For easy understanding, examples of three different oriented grains, G1, G2 and G3, are illustrated to show how the point locations in the standard stereographic triangle correlate to the actual grains in optical microscope image and EBSD orientation map.

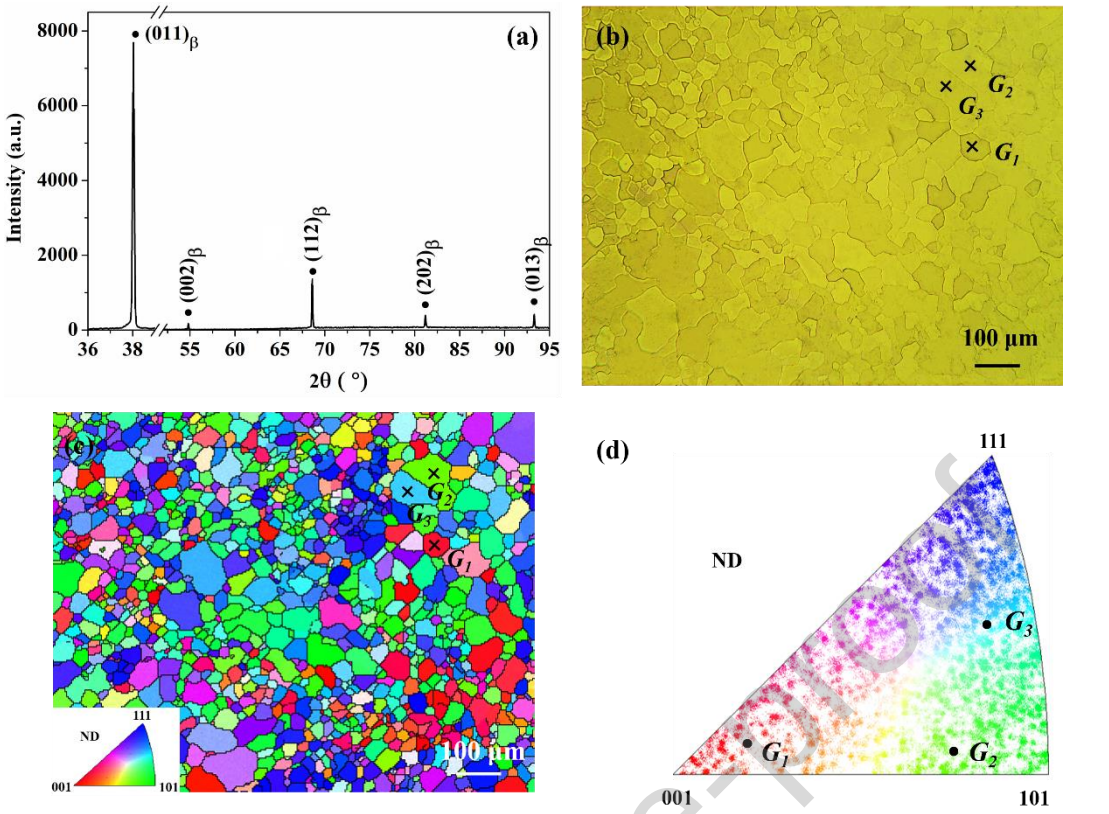

Fig. 1 (a) XRD pattern, (b) optical microscope image, (c) EBSD orientation map and (d) inverse pole figure (IPF) in surface normal direction (ND) obtained from the same area in Ti2033 alloy.

3.2 Nanoindentation load-displacement curves

Fig. 2 shows the normalized load-displacement (*F*-*h*) curves for grains oriented in <001>$_\beta$, <101>$_\beta$, and <111>$_\beta$, respectively. The maximum indentation load was controlled respectively at F_m = 60 mN for the Sp50 indenter and at F_m = 10 mN for the Bkv indenter, so as to obtain an approximately equivalent maximum indentation depth h_m for both indenters ($h_m \approx$ 300 nm). Normalized nanoindentation curves were obtained from the raw load-displacement (*F*-*h*) curves by scaling the load and depth by their respective maximum load F_m and maximum depth h_m. Normalized F/F_m - h/h_m curves gives more sensitivity to unloading curves and enable a direct reading of η_h values which correspond to the x-intercepts of unloading curves, as indicated in Fig. 2a. The depth recovery ratio η_h is defined as the recoverable depth divided by the maximum depth h_m. The work recovery ratio η_w is defined as the ratio of recoverable work to the total work and is represented by the area enclosed between the normalized unloading curve, the y=1 vertical line and the x axis. Normalized *F*-*h* curves allow to emphasize the orientation dependence of η_h and η_w ratios.

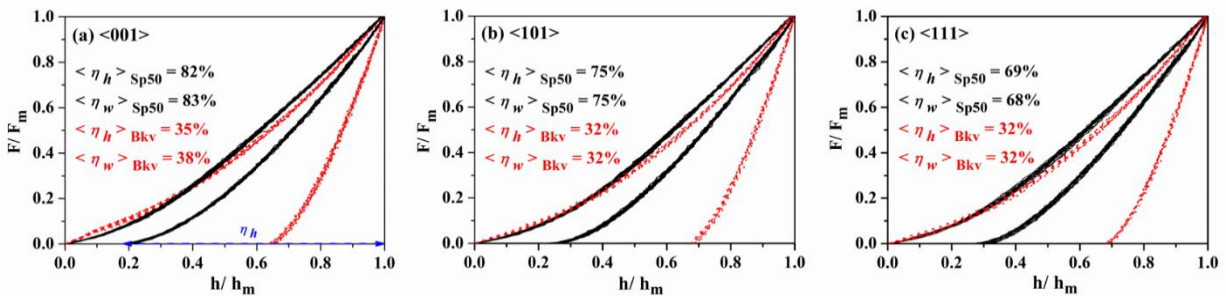

Fig. 2 Normalized F/F_m - h/h_m nanoindentation curves of Sp50 (continuous curves) and Bkv (dotted curves) indentations applied on: (a) <001> crystals, (b) <101> crystals, and (c) <111> crystals.

When indenting with the Sp50 indenter, the recoverability is highly dependent on the crystallographic orientation of the indented grain: η_h and η_w for grains orientated in the $<001>_\beta$ direction, noted $\eta_{h\ <001>}$ and $\eta_{w\ <001>}$, have the largest values of 82% and 83%, respectively, as compared to $\eta_{h\ <101>}$ and $\eta_{w\ <101>}$ that present intermediate values of 75% and 75%, and $\eta_{h\ <111>}$ and $\eta_{w\ <111>}$ that display the lowest values of 69% and 68%. For the Bkv indenter, recovery ratios are relatively low (~32%), with no significant orientation-dependence. The characteristic of unloading curves is closely associated with the recoverability and reflects the deformation mechanisms underneath the indenters. Bkv indenter produces sudden high stresses, leads to an immediate onset of plasticity, and subsequently causes extremely steep unloading curves [20], whereas spherical indentations exhibit gentle and soft unloading curves, suggesting the occurrence of strain accommodation by reversible phase transformation [22]. It is noteworthy that measurements of recoverability (η_h and η_w) by nanoindentation demonstrate high reproducibility. For instance, using Sp50 indenter, the means values of depth recovery ratio $<\eta_h>$ for each principal direction show very small mean standard deviations of 1.04 %, 0.93 %, and 1.38% for the $<001>_\beta$, $<101>_\beta$, and $<111>_\beta$ directions, respectively.

3.3 Anisotropy of depth and work recovery ratios

To present the crystallographic anisotropy of the superelasticity, depth- and work-recovery ratios of Sp50 and Bkv indentations measured from individual grains were presented in standard stereographic triangles in Fig. 3. With this representation, it is clearly observed that η_h and η_w values are indeed influenced by the crystallographic orientations. For both indenters, grains orientated in the $<001>_\beta$ direction exhibit the largest η_h and η_w values, and followed by those of grains oriented in the $<101>_\beta$ and $<111>_\beta$ directions. Besides, the η_h and η_w values for Sp50 indenter are higher than those for the Bkv indenter in all directions.

Specifically, the values of η_h and η_w for the Sp50 indenter vary in the ranges of 66% - 85% and 67% - 86%, respectively, for which the ranges are approximately twice of those for the Bkv indenter with η_h varying from 29% to 40% and η_w from 31% to 38%, respectively. The larger dispersion ranges (Δ (max-min)) of η_h and η_w values obtained with the Sp50 indenter suggest that spherical indentations are more sensitive to the crystallographic loading direction when compared to the Bkv indentations. It confirms that the spherical nanoindentation is capable of characterizing the crystallographic anisotropy of the depth- and work- recoverability involving reversible stress-induced martensitic (SIM) transformation in superelastic alloys.

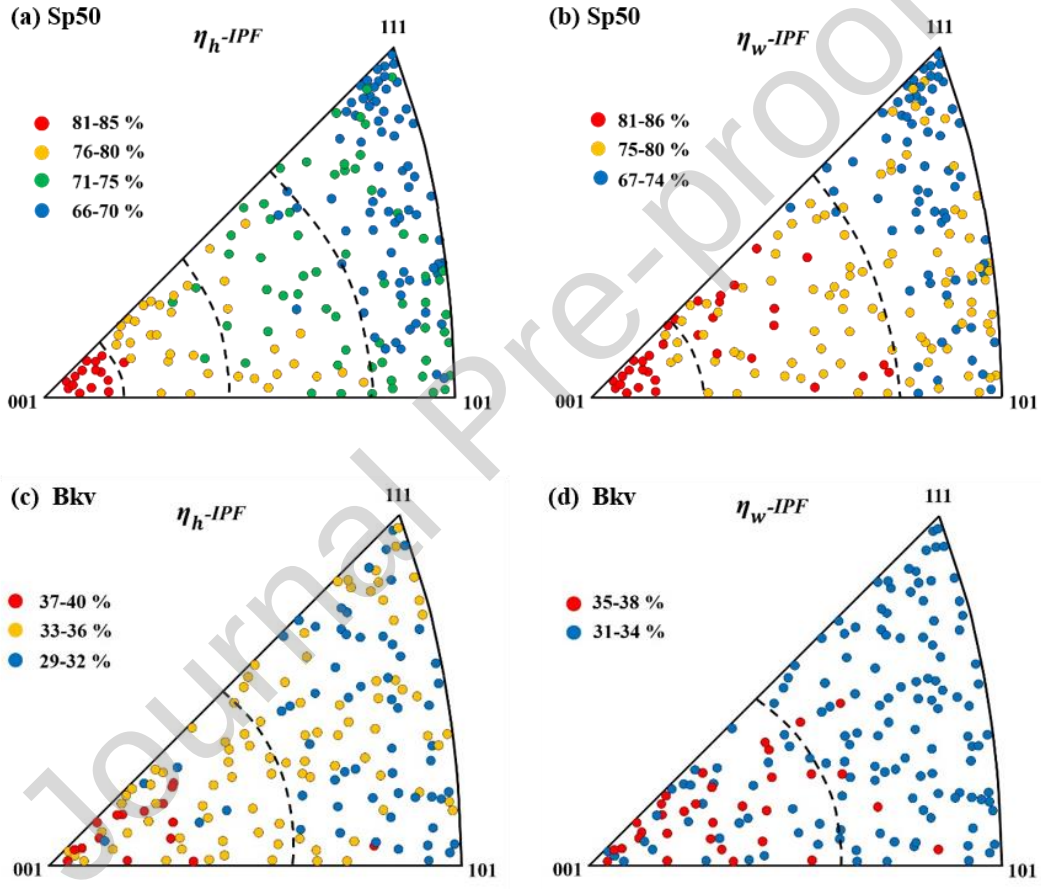

Fig. 3 *ηh - IPF* and *ηw - IPF* measured with: (a, b) Sp50 indenter and (c, d) Bkv indenter.

The different nanoindentation behaviors probed using two different indenters is strongly related to the geometry of the indenter tips. Indenting with the Sp50 indenter clearly displays higher recoverability evidencing the superelasticity, whereas Bkv indentations result in more pronounced plastic deformation. The sharp Bkv indenter generates high strain which cannot be accommodated by elastic deformation and stress-induced martensitic transformation (superelastic deformation), so that plastic deformation through dislocation motions is the predominant deformation mechanism under Bkv indenter [23, 24]. In the case of Bkv

indentations, their η_h and η_w values vary narrowly with respect to crystal orientations. It could be argued that plastic deformation of β phase seems not sensitive to crystallographic direction. The SIM transformation competes with the dislocation motions. The generation of dislocations, on one hand, is not desirable for the occurrence of SIM transformation from β phase to α″ phase, and on the other hand, impedes the reverse transformation from α″ phase to the parent β phase, resulting in a low recoverability. In contrast, the strain field developed underneath the Sp50 indenter is more likely to favor larger martensitic transformation and facilitate the capture of the superelastic nature in metastable β Ti2033 alloy. Therefore, it can be concluded here that the indenters in different geometries generate different strain level, and reveal different amount of elastic, superelastic and plastic deformation, showing the characteristics of different magnitudes of indentation recovery ratios for spherical and Bkv indentations.

It is well established that the superelasticity nature in β-Ti alloys arises from the reversible martensitic transformation between the bcc structure of the parent β phase and the C-centered orthorhombic structure of the stress-induced α'' martensite [21, 25-27]. The formation of α'' phase from a β crystal follows the orientation relationships [28]: $\{100\}_{\beta}$ // $(100)_{\alpha''}$, and $<111>_{\beta}$ // $[110]_{\alpha''}$. Six lattice correspondence variants Vi (i = 1 to 6) can be defined from the orientation relationship, as shown in Fig. 4. It is commonly assumed that the variant that would accommodate maximum strain along the loading direction (compression or tension) would produce maximum driving force for the martensitic transformation and would thus be preferentially formed in each grain [1, 4, 29]. Thus, the formation of the favorable variants of stress-induced martensite is dependent on the loading direction. It also suggests that superelastic effect is orientation-dependent. The theoretical maximum value of transformation strain which can be obtained along a given crystallographic direction of the β phase is consisted with the maximum lattice deformation strain that can be obtained along this direction.

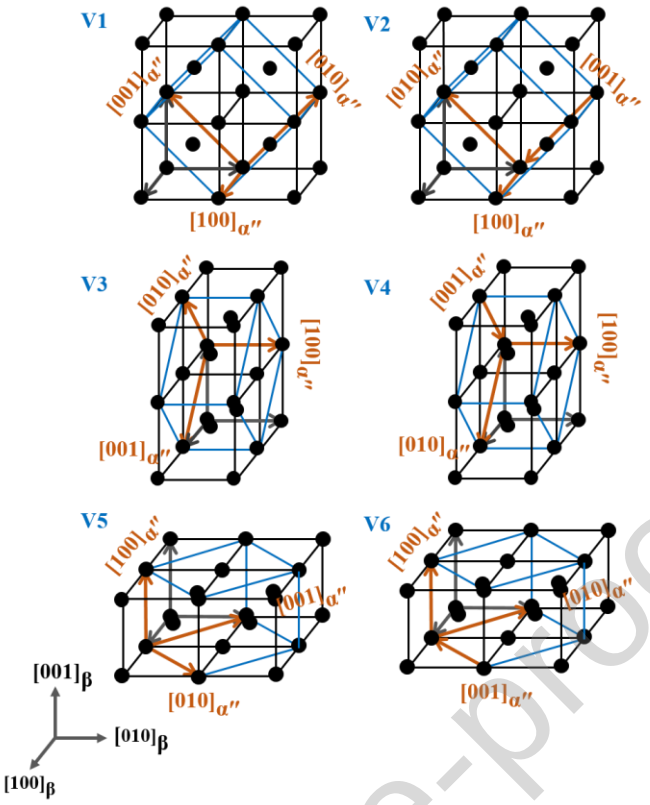

Fig. 4 The six lattice correspondences between the bcc structure of the β phase and the orthorhombic structure of α″ martensite phase.

When a given vector X in the coordinates of the parent β phase is transformed to X' in the coordinates of α" phase through martensitic transformation (Fig. 4), the transformation strain of each variant $\varepsilon_{\beta\to\alpha''}^{(Vi)}$ is calculated by [30, 31]:

$$\varepsilon_{\beta\to\alpha''}^{(\mathrm{Vi})} = \frac{|X'^{(Vi)}|-|X|}{|X|} \tag{1}$$

where $X'^{(Vi)} = T^{(Vi)}X$, and $\mathrm{T}^{(\mathrm{Vi})}$ represents the lattice distortion matrix expressed in the coordinates of the parent β phase for each martensitic variant. The superelastic recovery is related to the transformation strain which arises from geometric lattice distortions between the β and α″ crystals. Therefore, the transformation strain can be calculated using the lattice parameters of β and α" phases, and their lattice correspondences. Lattice parameters calculated using unit-cell refinement software with the data from the XRD pattern of magnetron-sputtered Ti2033 film elaborated in our lab (in press) were used for the transformation strain calculations of Ti2033 alloys: a_β = 3.395 Å, $a_{\alpha''}$ = 3.219 Å, $b_{\alpha''}$ = 5.008 Å, and $c_{\alpha''}$ = 4.874 Å. It is noted that the lattice parameters of β and α″ phases in Ti2033 film were used, rather than those of Ti2033 bulk measured by synchrotron XRD during tensile test [21]. The reason is that the formation of α″ phase in Ti2033 bulk during tensile test is

activated in tension, whereas the α″ phase in Ti2033 film is compression-stress-induced since magnetron-sputtered films elaborated at low sputtering pressure generally exhibit compressive stress due to the atomic peening mechanism [32]. Nanoindentation closely tends to produce compression loading condition in some sense, so that the martensitic transformation is induced in compression, which makes it more reasonable to use the lattice parameters of Ti2033 film for the calculation of transformation strain in order to rationalize the nanoindentation responses in the present work.

Fig. 5a shows the coordinate system employed for calculations of transformation strain $\varepsilon_{\beta\rightarrow\alpha''}^{(Vi)}$ along different loading directions. The angle θ denotes the angle between $[001]_\beta$ direction and the loading direction. Thus, when θ is equal to 0°, 54.74° or 90°, the loading direction refers to $[001]_\beta$, $[111]_\beta$, or $[110]_\beta$ crystallographic directions of the β phase, respectively. Fig. 5b shows the transformation strain $\varepsilon_{\beta\rightarrow\alpha''}^{(Vi)}$ calculated for each variant as a function of θ angle. The sign of the transformation strain $\varepsilon_{\beta\rightarrow\alpha''}^{(Vi)}$ implies the strain states under which the β→α″ transformation occurs: positive values for tensile strain state and negative ones for compressive strain state. It is observed that there is a pronounced difference in the magnitude of transformation strain in tension and compression for a given loading direction, suggesting a strong tension-compression asymmetry in the strain response. This asymmetry phenomenon was commonly observed during uniaxial tests in superelastic β titanium textured alloys [5, 33] and in NiTi alloys [34-36].

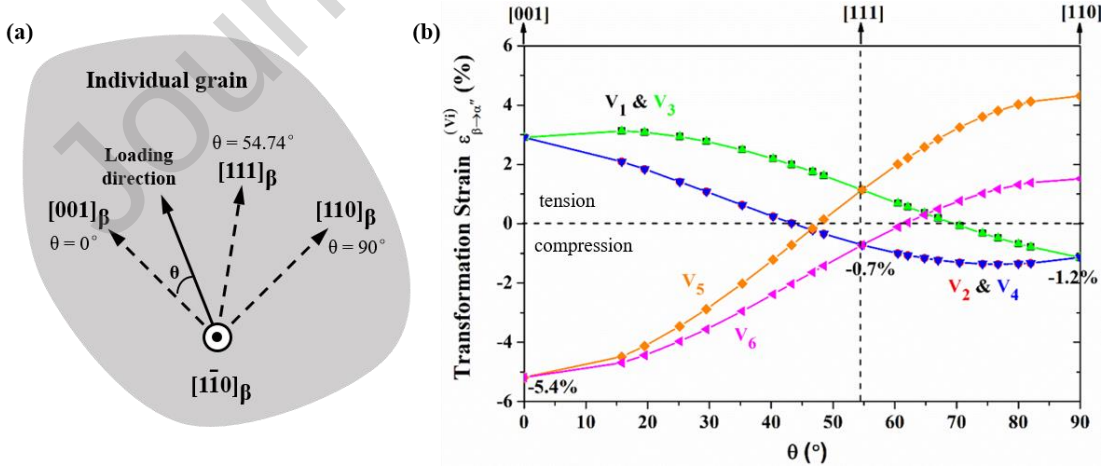

Fig. 5 (a) Schematic illustration of the coordinate system employed for calculations of transformation strain. The angle θ denotes the angle between the loading direction and $[001]_\beta$ direction in the considered β grain oriented in $[1\bar{1}0]_\beta$. (b) Transformation strain $\varepsilon_{\beta\rightarrow\alpha''}^{(Vi)}$ of each variant as a function of θ angle.

More focus is on the negative values of $\varepsilon_{\beta\rightarrow\alpha''}^{(Vi)}$ (half-below y-axis) which represents the theoretical compressive strains that can be accommodated during compressive-stress-induced martensitic transformation in Ti2033 alloy. Although nanoindentation test is different as compared to compressive uniaxial tests, it is likely in the same sense that compressive strain field is developed when the indenter is pressed into the material surface during nanoindentation. As can be seen from Fig. 5b, the transformation strain evolves with θ. When the indentation loading direction is along the $[001]_\beta$ (θ = 0°), V5 and V6 variants have the largest magnitude of $\varepsilon_{\beta\rightarrow\alpha''}^{(Vi)}$ (5.4%), and thus can be preferentially indentation-induced, showing the potential to obtain a large superelastic recovery. When the loading direction is along $[111]_\beta$ (θ = 54.74°) and $[110]_\beta$ (θ = 90°), the magnitudes of $\varepsilon_{\beta\rightarrow\alpha''}^{(Vi)}$ are comparable at 0.7% and 1.2%, respectively. Transformation strain calculations show the crystallographic anisotropy of martensitic transformation through the existence of the six martensite variants.

To comprehensively show the orientation dependence of the transformation strain, the $\varepsilon_{\beta\rightarrow\alpha''}^{(Vi)}$ were calculated for 85 representative orientations located in the [001]-[101]-[111] standard stereographic triangle. Among the negative values of calculated $\varepsilon_{\beta\rightarrow\alpha''}^{(Vi)}$ for a given direction, the one with the largest magnitute was recorded as the theoretical maximum transformation strain under compression for this considered direction and was presented correspondingly in the standard stereographic triangle in Fig. 6. It is shown that the grains oriented in $<001>_\beta$ direction exhibit the maximum transformation strain of 5.4%, and it decreases as the orientation changes from $<001>_\beta$ towards $<101>_\beta$ and $<111>_\beta$ directions, as indicated by the contour lines in Fig. 6.

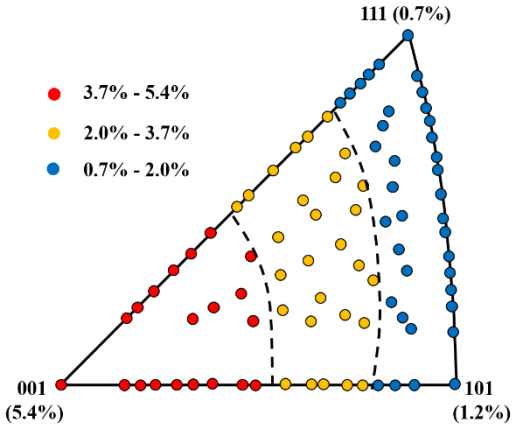

Fig. 6 Orientation dependence of the calculated maximum transformation strain associated with the

indentation-induced martensitic transformation from the β to α″ phases in Ti2033 alloy.

It is clearly observed that transformation strain calculations and experimental η_h and η_w measurements are in good qualitative agreement following the same trend. That is, the crystallographic anisotropy of the recoverability in η_h - *IPF* and η_w -*IPF* can be rationalized by the calculations of maximum transformation strain under compression on the basis of the crystallographic orientation relationship of the martensitic transformation in β -Ti alloys. Therefore, it is reasonable to accept that the η_h - and η_w - IPF distributions can capture and reflect the crystallographic anisotropy of the superelasticity.

3.4 Anisotropy of the indentation modulus

Fig. 7 shows the distribution of the indentation modulus, E_{IT} - *IPF,* for the Sp50 and Bkv indenters. According to color scales, the IPFs were scaled into 3 sections with the dashed lines. The colored points distributed within the IPF triangles for the two indenters follow the same trend: the grains orientated in $<001>_\beta$ and $<111>_\beta$ crystallographic directions exhibit the lowest and largest values, respectively, and grains orientated in $<101>_\beta$ direction fall in the intermediate, which suggests the orientation dependence of E_{IT}. For a given orientation, the E_{IT} value for Bkv indenter was observed to be lower than that for Sp50 indenter, which is consistent with the results reported for pure titanium [37] and Ti2448 alloy [20].

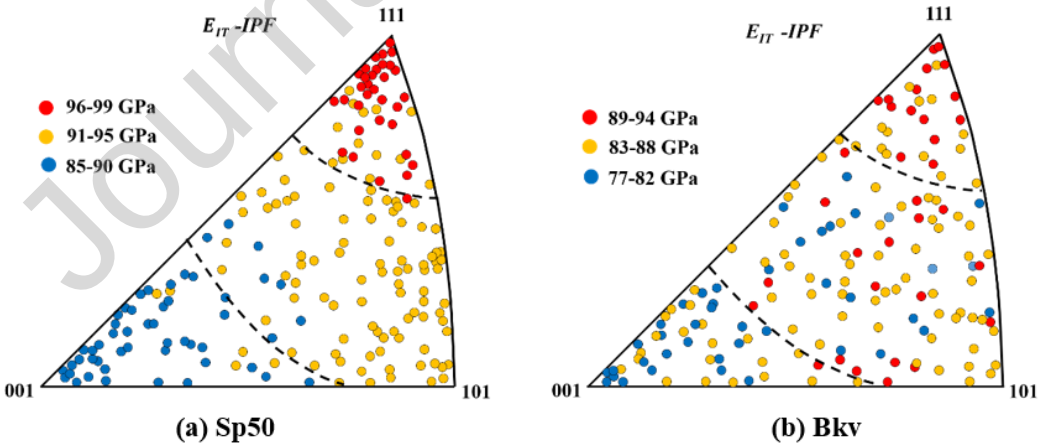

Fig. 7 Indentation modulus inverse pole figures (E_{IT}-*IPF*) measured with: (a) the Sp50 indenter and (b) the Bkv indenter.

The orientation dependence of indentation modulus E_{IT} can be qualitatively analyzed from the crystallographic anisotropy of calculated Young's modulus. A cubic crystal can be characterized by only three independent elastic constants (c_{11}, c_{12} and c_{44}) due to the strong cubic symmetry. For all classes of cubic crystals, Young's modulus E_{hkl} in any

crystallographic direction [*h k l*] can be calculated by the following equation [38-40]:

$$E_{hkl} = \left\{ \frac{c_{11}+c_{12}}{(c_{11}-c_{12})(c_{11}+2c_{12})} + \left(\frac{1}{c_{44}} - \frac{2}{c_{11}-c_{12}} \right) \frac{(h^2k^2+h^2l^2+k^2l^2)}{(h^2+k^2+l^2)^2} \right\}^{-1} \quad (2)$$

It is worth noting that the Young's modulus corresponds to uniaxial testing conditions while the indentation modulus is obtained from rather more complex loading conditions with triaxial stress state. The neglect of the triaxial stress state under the indenter introduces some difficulties to clearly determine the real local Young's modulus. Nevertheless, the objective of this work was focused on evolution tendency of elastic modulus with respect to the crystallographic orientations, rather than the determination of the absolute value of this local elastic property. Comparison of the values of the Young's and indentation moduli deserves further research. Thus, indentation modulus evolution could be roughly correlated with the evolution of Young's modulus. For a grain orientated in <*h k l*> direction aligned with the loading axis, the Young's modulus E_{hkl} can be deduced from Eq. 2. The elastic constants of Ti-22Zr alloy, c_{11} = 109.2 GPa, c_{12} = 98.9 GPa and c_{44} = 14.3 GPa [41], were used for the calculation of theoretical Young's modulus and were considered for discussion and comparison with indentation moduli measured in our Ti2033 alloy.

Fig. 8 shows the inverse pole figure distribution of calculated Young's modulus for Ti-22Zr β crystal. The crystallographic orientation dependence is obviously demonstrated as indicated by the ranges bounded by dashed lines. The IPF distribution of calculated Young's modulus shows a decreasing trend as the crystallographic orientation of grains changes from $<111>_{\beta}$ towards the $<101>_{\beta}$ and $<001>_{\beta}$, which is in a good qualitative agreement with the nanoindentation measurements in Fig. 7. The observed orientation dependence in Ti2033 is consistent with that calculated from the measured elastic stiffness in Ti-29Nb-Ta-Zr and Ti-25Nb-Ta-Zr single crystals [42]. Indentation moduli measured by nanoindentation are likely to be overestimated compared to Young's moduli calculated with elastic constants, which is probably due to the overestimation of the true contact area [43, 44]. Accurate determination of the rue contact area during post-experiment using imaging techniques can be employed only if elastic recovery is negligible, which is not the present case.

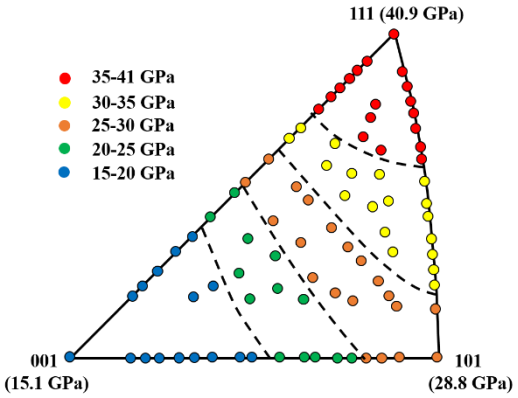

Fig. 8 Orientation dependence of Young's modulus calculated from elastic constants of Ti-22Zr alloy.

3.5 Indentation hardness

Fig. 9 shows the indentation hardness inverse pole figure (H_{IT} -IPF) measured with the Sp50 and Bkv indenters. In contrast to the inverse pole figure distributions of η_h, η_w E_{IT}, no significant trend was found for H_{IT} values as a function of the crystallographic orientation for both indenters, suggesting that H_{IT} is orientation-independent. Similar result has been reported in polycrystalline β Ti-Al alloys where no obvious change was identified for indentation hardness of β grains [45]. It is related to the bcc structure of the β grains which can contain 48 possible slip systems. In β-Ti alloys, slip planes are observed to be {110}, {112} or {123} planes and several slip systems are frequently observed to operate simultaneously in the same grain [46, 47]. Thus, the isotropic distribution of H_{IT} values of the Ti2033 alloy can be ascribed to the active dislocation activity in bcc crystals. It is different from the observations in pure α-Ti with hexagonal structure that indentation hardness varied significantly with crystal orientation: indentation hardness for individual grains orientated in [0001] direction exhibited the highest value, then decreased as the orientations deviated from the [0001] direction [8, 37, 48]. This is due to a strong anisotropy of slip systems in hcp α-Ti structure.

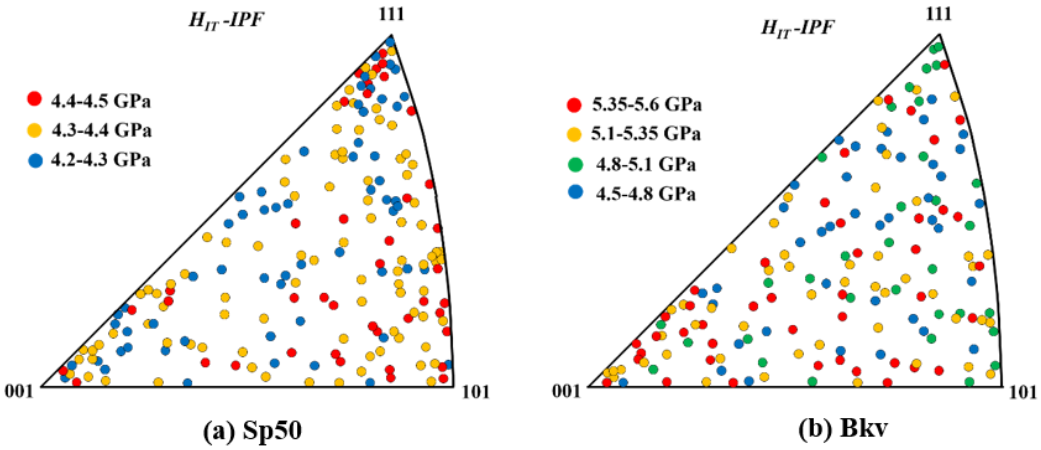

Fig.9 Indentation hardness inverse pole figures (H_{IT}-*IPF*) measured with: (a) the Sp50 indenter and (b) the Bkv indenter.

4 Conclusion

In the present study, the superelastic Ti2033 alloy was investigated by nanoindentation and EBSD in order to shed lights on the crystallographic anisotropy of indentation responses. The main conclusions were made as follows:

(1) The crystallographic anisotropy of the superelasticity revealed in η_h - *IPF* and η_w -*IPF* can be rationalized by the calculations of maximum transformation strain under compression on the basis of the crystallographic orientation relationship of the martensitic transformation in β-Ti alloys. Therefore, it is reasonable to accept that the nanoindentation η_h - and η_w - IPF distributions can capture and reflect the crystallographic anisotropy of the superelasticity.

(2) Indentation modulus E_{IT} exhibited orientation dependence for both Sp50 and Bkv indenters. The IPF distributions of the indentation modulus were qualitatively similar to the one predicted by calculations of Young's modulus from the measured elastic constants. No crystallographic anisotropy of indentation hardness was detected, due to multiple slip systems activated in the bcc β crystal.

(3) Indentation responses were strongly determined by the indenter geometry. Spherical nanoindentation is more appropriate to capture the superelastic nature of materials and probe crystallographic anisotropy of the indentation responses, due to the strain distribution field generated under the Sp50 indenter which is smoothly distributed and more favorable for the martensitic transformation (superelastic deformation), as compared to the case of sharp Bkv indenter.

Acknowledgements

Y. Zhou acknowledges the China Scholarship Council (CSC) for her Ph.D financial support (No. 201701810085). The authors also acknowledge the SCANMAT platform of the University of Rennes for providing access to SEM facilities.

References

[1] T. Inamura, Y. Fukui, H. Hosoda, K. Wakashima, S. Miyazaki, Relationship between Texture and Macroscopic Transformation Strain in Severely Cold-Rolled Ti-Nb-Al Superelastic Alloy, Materials Transactions, 45 (2004) 1083-1089.

[2] Y. Chai, H. Kim, H. Hosoda, S. Miyazaki, Self-accommodation in Ti–Nb shape memory alloys, Acta materialia, 57 (2009) 4054-4064.

[3] H.Y. Kim, S. Miyazaki, Martensitic transformation and superelastic properties of Ti-Nb base alloys, Materials Transactions, 56 (2015) 625-634.

[4] H.Y. Kim, T. Sasaki, K. Okutsu, J.I. Kim, T. Inamura, H. Hosoda, S. Miyazaki, Texture and shape memory behavior of Ti–22Nb–6Ta alloy, Acta Materialia, 54 (2006) 423-433.

[5] Y.W. Zhang, S.J. Li, E.G. Obbard, H. Wang, S.C. Wang, Y.L. Hao, R. Yang, Elastic properties of Ti–24Nb–4Zr–8Sn single crystals with bcc crystal structure, Acta Materialia, 59 (2011) 3081-3090.

[6] C.P. Frick, S. Orso, E. Arzt, Loss of pseudoelasticity in nickel–titanium sub-micron compression pillars, Acta Materialia, 55 (2007) 3845-3855.

[7] C.P. Frick, B.G. Clark, S. Orso, P. Sonnweber-Ribic, E. Arzt, Orientation-independent pseudoelasticity in small-scale NiTi compression pillars, Scripta Materialia, 59 (2008) 7-10.

[8] T. Britton, H. Liang, F. Dunne, A. Wilkinson, The effect of crystal orientation on the indentation response of commercially pure titanium: experiments and simulations, Proceedings of the Royal Society A: Mathematical, Physical and Engineering Sciences, 466 (2010) 695-719.

[9] C. Tromas, J.-C. Stinville, C. Templier, P. Villechaise, Hardness and elastic modulus gradients in plasma-nitrided 316L polycrystalline stainless steel investigated by nanoindentation tomography, Acta Materialia, 60 (2012) 1965-1973.

[10] C. Tromas, M. Arnoux, X. Milhet, Hardness cartography to increase the nanoindentation resolution in heterogeneous materials: Application to a Ni-based single-crystal superalloy, Scripta Materialia, 66 (2012) 77-80.

[11] C.P. Frick, T.W. Lang, K. Spark, K. Gall, Stress-induced martensitic transformations and shape memory at nanometer scales, Acta Materialia, 54 (2006) 2223-2234.

[12] G. Laplanche, J. Pfetzing-Micklich, G. Eggeler, Sudden stress-induced transformation events during nanoindentation of NiTi shape memory alloys, Acta Materialia, 78 (2014) 144-160.

[13] S. Pathak, S.R. Kalidindi, Spherical nanoindentation stress–strain curves, Materials Science and Engineering: R: Reports, 91 (2015) 1-36.

[14] S. Kumar, I.A. Kumar, L. Marandi, I. Sen, Assessment of small-scale deformation characteristics and stress-strain behavior of NiTi based shape memory alloy using nanoindentation, Acta Materialia, 201 (2020) 303-315.

[15] A.M. Wood, J.-H. You, T. Clyne, Nanoindention response of superelastic materials, in: Smart Materials III, International Society for Optics and Photonics, 2004, pp. 216-223.

[16] H.-S. Zhang, K. Komvopoulos, Nanoscale pseudoelasticity of single-crystal Cu–Al–Ni shape-memory alloy induced by cyclic nanoindentation, Journal of materials science, 41 (2006) 5021-5024.

[17] C.-Y. Nien, H.-K. Wang, C.-H. Chen, S. Ii, S.-K. Wu, C.-H. Hsueh, Superelasticity of TiNi-based shape memory alloys at micro/nanoscale, Journal of Materials Research, 29 (2014) 2717-2726.

[18] J. Pfetzing, A. Schaefer, C. Somsen, M.F.-X. Wagner, Nanoindentation of pseudoelastic NiTi shape memory alloys: thermomechanical and microstructural aspects, International journal of materials research, 100 (2009) 936-942.

[19] J. Pfetzing-Micklich, M.F.X. Wagner, R. Zarnetta, J. Frenzel, G. Eggeler, A.E. Markaki, J. Wheeler, T.W. Clyne, Nanoindentation of a pseudoelastic NiTiFe shape memory alloy, Advanced Engineering Materials, 12 (2010) 13-19.

[20] H. Jabir, A. Fillon, P. Castany, T. Gloriant, Crystallographic orientation dependence of mechanical properties in the superelastic Ti-24Nb-4Zr-8Sn alloy, Physical Review Materials, 3 (2019) 063608.

[21] J.J. Gao, I. Thibon, D. Laillé, P. Castany, T. Gloriant, Influence of texture and transformation strain on the superelastic performance of a new Ti–20Zr–3Mo–3Sn alloy, Materials Science and Engineering: A, 762 (2019) 138075.

[22] Y. Zhou, A. Fillon, H. Jabir, D. Laillé, T. Gloriant, Investigation of the superelastic behavior of a Ti-16Zr-13Nb-2Sn sputtered film by nanoindentation, Surface and Coatings Technology, (2020) 126690.

[23] G. Pan, Z. Cao, J. Shi, M. Wei, L. Xu, X. Meng, Different mechanical response of TiNi film induced by the shape of indenter during nanoindentation, Sensors and Actuators A: Physical, 217 (2014) 75-80.

[24] W. Ni, Y.-T. Cheng, D.S. Grummon, Microscopic superelastic behavior of a nickel-titanium alloy under complex loading conditions, Applied Physics Letters, 82 (2003) 2811-2813.

[25] Y. Yang, P. Castany, M. Cornen, I. Thibon, F. Prima, T. Gloriant, Texture investigation of the superelastic Ti–24Nb–4Zr–8Sn alloy, Journal of Alloys and Compounds, 591 (2014) 85-90.

[26] Y. Yang, P. Castany, M. Cornen, F. Prima, S.J. Li, Y.L. Hao, T. Gloriant, Characterization of the martensitic transformation in the superelastic Ti–24Nb–4Zr–8Sn alloy by in situ synchrotron X-ray diffraction and dynamic mechanical analysis, Acta Materialia, 88 (2015) 25-33.

[27] Y. Yang, P. Castany, Y. Hao, T. Gloriant, Plastic deformation via hierarchical nano-sized martensitic

twinning in the metastable β Ti-24Nb-4Zr-8Sn alloy, Acta Materialia, 194 (2020) 27-39.

[28] T. Duerig, J. Albrecht, D. Richter, P. Fischer, Formation and reversion of stress induced martensite in Ti-10V-2Fe-3Al, Acta Metallurgica, 30 (1982) 2161-2172.

[29] M. Tahara, H.Y. Kim, T. Inamura, H. Hosoda, S. Miyazaki, Lattice modulation and superelasticity in oxygen-added β-Ti alloys, Acta materialia, 59 (2011) 6208-6218.

[30] H. Kim, Y. Ikehara, J.I. Kim, H. Hosoda, S. Miyazaki, Martensitic transformation, shape memory effect and superelasticity of Ti–Nb binary alloys, Acta Materialia, 54 (2006) 2419-2429.

[31] H.Y. Kim, J. Fu, H. Tobe, J.I. Kim, S. Miyazaki, Crystal structure, transformation strain, and superelastic property of Ti–Nb–Zr and Ti–Nb–Ta alloys, Shape memory and Superelasticity, 1 (2015) 107-116.

[32] J.A. Thornton, D.W. Hoffman, Internal stresses in titanium, nickel, molybdenum, and tantalum films deposited by cylindrical magnetron sputtering, Journal of Vacuum Science and Technology, 14 (1977) 164-168.

[33] Z. Zhang, Y. Hao, S. Li, R. Yang, Fatigue behavior of ultrafine-grained Ti–24Nb–4Zr–8Sn multifunctional biomedical titanium alloy, Materials Science and Engineering: A, 577 (2013) 225-233.

[34] K. Gall, H. Sehitoglu, Y.I. Chumlyakov, I.V. Kireeva, Tension–compression asymmetry of the stress–strain response in aged single crystal and polycrystalline NiTi, Acta Materialia, 47 (1999) 1203-1217.

[35] K. Gall, H. Sehitoglu, The role of texture in tension–compression asymmetry in polycrystalline NiTi, International Journal of Plasticity, 15 (1999) 69-92.

[36] S.C. Mao, J.F. Luo, Z. Zhang, M.H. Wu, Y. Liu, X.D. Han, EBSD studies of the stress-induced B2–B19′ martensitic transformation in NiTi tubes under uniaxial tension and compression, Acta Materialia, 58 (2010) 3357-3366.

[37] C. Fizanne-Michel, M. Cornen, P. Castany, I. Péron, T. Gloriant, Determination of hardness and elastic modulus inverse pole figures of a polycrystalline commercially pure titanium by coupling nanoindentation and EBSD techniques, Materials Science and Engineering: A, 613 (2014) 159-162.

[38] L. Zhang, R. Barrett, P. Cloetens, C. Detlefs, M. Sanchez del Rio, Anisotropic elasticity of silicon and its application to the modelling of X-ray optics, Journal of Synchrotron Radiation, 21 (2014) 507-517.

[39] J.-M. Zhang, Y. Zhang, K.-W. Xu, V. Ji, Young's modulus surface and Poisson's ratio curve for cubic metals, Journal of Physics and Chemistry of Solids, 68 (2007) 503-510.

[40] J.J. Wortman, R.A. Evans, Young's Modulus, Shear Modulus, and Poisson's Ratio in Silicon and

Germanium, Journal of Applied Physics, 36 (1965) 153-156.

[41] C.A. Salvador, B.F. Zornio, C.R. Miranda, Discovery of Low-Modulus Ti-Nb-Zr Alloys Based on Machine Learning and First-Principles Calculations, ACS Applied Materials & Interfaces, (2020).

[42] M. Tane, S. Akita, T. Nakano, K. Hagihara, Y. Umakoshi, M. Niinomi, H. Nakajima, Peculiar elastic behavior of Ti–Nb–Ta–Zr single crystals, Acta Materialia, 56 (2008) 2856-2863.

[43] R.A. Mirshams, R.M. Pothapragada, Correlation of nanoindentation measurements of nickel made using geometrically different indenter tips, Acta Materialia, 54 (2006) 1123-1134.

[44] G.B. Viswanathan, E. Lee, D.M. Maher, S. Banerjee, H.L. Fraser, Direct observations and analyses of dislocation substructures in the α phase of an α/β Ti-alloy formed by nanoindentation, Acta Materialia, 53 (2005) 5101-5115.

[45] X. Lei, L. Dong, Z. Zhang, M. Hu, Z. Wang, Y. Hao, R. Yang, Microtexture and nanoindentation of α and β Phases in Ti–6Al–1.5 Cr–2.5 Mo–0.5 Fe–0.3 Si titanium alloy, Science of Advanced Materials, 9 (2017) 1476-1483.

[46] P. Castany, M. Besse, T. Gloriant, Dislocation mobility in gum metal β-titanium alloy studied via in situ transmission electron microscopy, Physical Review B, 84 (2011) 201-201 - 201-204.

[47] P. Castany, M. Besse, T. Gloriant, In situ TEM study of dislocation slip in a metastable β titanium alloy, Scripta Materialia, 66 (2012) 371-373.

[48] C. Zambaldi, Y. Yang, T.R. Bieler, D. Raabe, Orientation informed nanoindentation of α-titanium: Indentation pileup in hexagonal metals deforming by prismatic slip, Journal of Materials Research, 27 (2011) 356-367.

CRediT authorship contribution statement

Ying Zhou: Methodology, Investigation, Writing- Original draft. **Amélie Fillon:** Methodology, Investigation, Writing Reviewing and Editing. **Denis Laillé:** Investigation, Resources. **Thierry Gloriant:** Methodology, Resources, Supervision.

Declaration of Competing Interest

☒ The authors declare that they have no known competing financial interests or personal relationships that could have appeared to influence the work reported in this paper.

☐The authors declare the following financial interests/personal relationships which may be considered as potential competing interests:

Graphical abstract

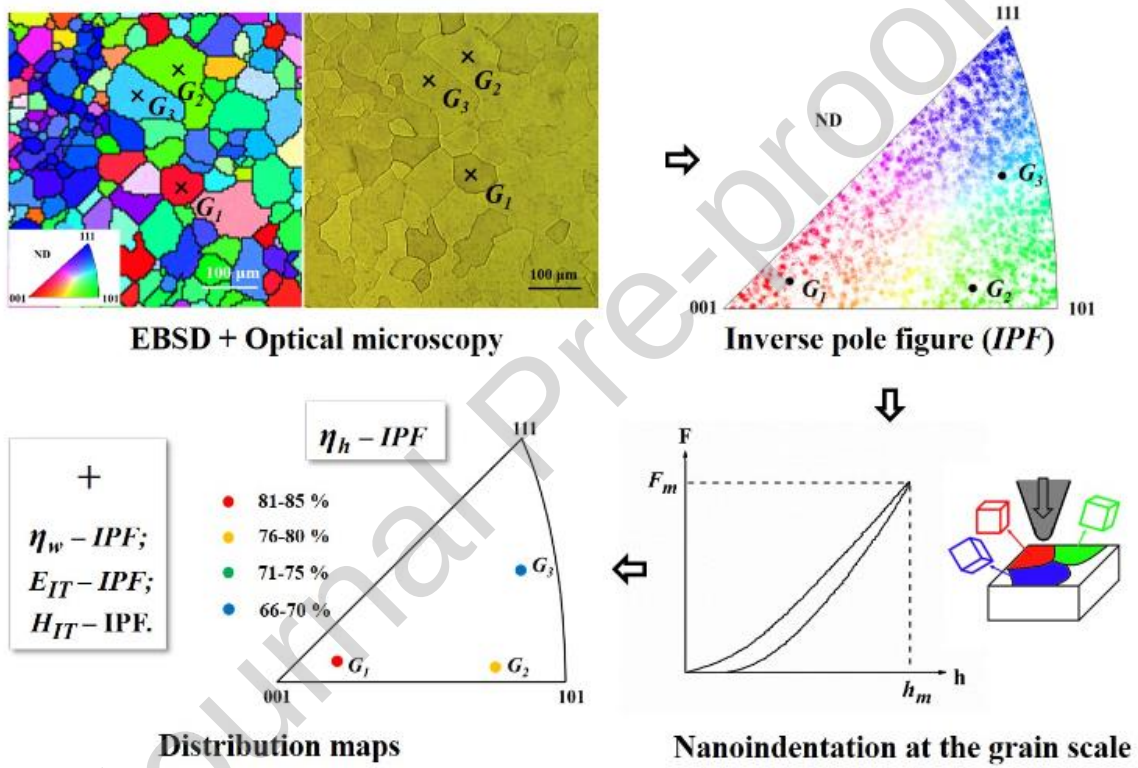

Highlights

- A strategy of combining nanoindentation with EBSD was proposed.
- Anisotropy of indentation responses was studied at individual grain scale.
- Anisotropy in superelasticity arises from anisotropy in β→α″ transformation strain.
- Indentation responses were strongly determined by the indenter geometry.
- Spherical nanoindentation is capable of probing the superelasticity of Ti alloys.